Exciton confinement in homo- and heteroepitaxial ZnO/$Zn_{1-x}Mg_xO$ quantum wells with $x < 0.1$

Bernhard Laumer,[1,2,a)] Thomas A. Wassner,[1] Fabian Schuster,[1] Martin Stutzmann,[1] Jörg Schörmann,[2] Marcus Rohnke,[3] Alexej Chernikov,[4] Verena Bornwasser,[4] Martin Koch,[4] Sangam Chatterjee,[4] and Martin Eickhoff[2]

[1]*Walter Schottky Institut, Technische Universität München, Am Coulombwall 4, 85748 Garching, Germany*
[2]*I. Physikalisches Institut, Justus-Liebig-Universität Gießen, Heinrich-Buff-Ring 16, 35392 Gießen, Germany*
[3]*Institut für Physikalische Chemie, Justus-Liebig-Universität Gießen, Heinrich-Buff-Ring 58, 35392 Gießen, Germany*
[4]*Faculty of Physics and Materials Science Center, Philipps-Universität Marburg, Renthof 5, 35032 Marburg, Germany*

(Received 1 June 2011; accepted 28 September 2011; published online 9 November 2011)

ZnO/$Zn_{1-x}Mg_xO$ single quantum well (SQW) structures with well widths d_W between 1.1 nm and 10.4 nm were grown by plasma-assisted molecular beam epitaxy both heteroepitaxially on c-plane sapphire and homoepitaxially on $(000\bar{1})$-oriented bulk ZnO. A significantly reduced Mg incorporation in the top barrier related to the generation of stacking faults is observed for heteroepitaxial samples. Exciton localization is observed for both types of samples, while an enhancement of the exciton binding energy compared to bulk ZnO is only found for homoepitaxial SQWs for 2 nm $\leq d_W \leq$ 4 nm. Consistently, for homoepitaxial samples, the carrier dynamics are mainly governed by radiative recombination and carrier cooling processes at temperatures below 170 K, whereas thermally activated non-radiative recombination dominates in heteroepitaxial samples. The effects of polarization-induced electric fields are concealed for Mg concentrations $x < 0.1$ due to the reduction of the exciton binding energy, the screening by residual carriers as well as the asymmetric barrier structure in heteroepitaxial wells. © *2011 American Institute of Physics*. [doi:10.1063/1.3658020]

I. INTRODUCTION

The ZnO/(ZnMg)O material system allows the fabrication of type-I heterostructures with large band offsets and direct optical transitions in the near ultraviolet spectral regime. By alloying with MgO, the bandgap can be tailored between 3.3 eV for pure ZnO and 4 eV for wurtzite $Zn_{1-x}Mg_xO$ with a Mg content of $x = 0.37$.[1,2] Thereby, the in-plane lattice parameter a for (0001)-oriented $Zn_{1-x}Mg_xO$ changes only moderately by 0.36 mÅ per percent of Mg incorporation,[1] allowing two-dimensional, pseudomorphic growth of $Zn_{1-x}Mg_xO$ thin films on ZnO with a layer thickness up to at least 38 nm for $x = 0.37$.[3] Several groups have investigated heteroepitaxial growth of ZnO/(ZnMg)O single heterostructures,[4–6] single quantum wells (SQWs),[7–15] double quantum wells,[16] and multiple quantum wells[17–19] on various substrates such as c-plane, a-plane, and r-plane sapphire, c-plane GaN/sapphire templates, Si(111), and $ScAlMgO_4$. However, only very few results of homoepitaxial growth of polar ZnO/(ZnMg)O SQWs have been reported,[20] although this growth technique can lead to improved structural, optical, and electrical properties of the resulting ZnO films.[21–23] In this paper, we compare the structural and optical properties of hetero- and homoepitaxially grown ZnO/$Zn_{1-x}Mg_xO$ single quantum well structures and discuss the role of exciton localization and of internal electric fields in SQWs with low Mg content.

II. EXPERIMENTAL DETAILS

ZnO/(ZnMg)O SQWs were grown by plasma-assisted molecular beam epitaxy (PAMBE) using double-zone Knudsen cells for the evaporation of Zn (6 N) and Mg (6 N), while oxygen (6 N) radicals were provided by a radiofrequency plasma source. ZnO template layers with a thickness of 300 nm were grown under stoichiometric growth conditions on c-plane sapphire at a substrate temperature of 460 °C employing an MgO/ZnO double buffer similar to the procedure described in Refs. 24 and 25. The resulting layers exhibited a root mean square (RMS) surface roughness of 0.4 nm on a 5 μm × 5 μm area. Next, two series of heteroepitaxial SQW samples with nominal well widths d_W between 1.3 nm and 10.4 nm and nominal barrier widths of 15 nm (20 nm) were deposited at a substrate temperature of 460 °C (540 °C) for series I (series II). The nominal well widths d_W were calculated according to the ZnO growth rate on c-plane sapphire for the corresponding growth conditions. Prior to growth of the homoepitaxial SQW structures (series III), $(000\bar{1})$-oriented bulk ZnO substrates[26] were annealed for 120 min at 1000 °C in O_2 atmosphere.[27] The SQW structures were grown simultaneously with those of series II except for the SQW with $d_W = 6.5$ nm. The Mg depth profile was studied by time-of-flight secondary ion mass spectroscopy (TOF-SIMS) using a TOF.SIMS 5-100 (iONTOF Company, Münster, Germany). The machine is equipped with a Bi-cluster primary ion gun and Caesium-, Oxygen-, and C_{60} -sputter guns. The analysis was carried out with single charged Bi-primary ions with energy of 25 keV. For the

a)Electronic mail: Bernhard.Laumer@wsi.tum.de.

sputtering, we chose 10 keV single charged C_{60} -ions. The field of analysis for each sample was 60 μm × 60 μm. The primary ion diameter determining the lateral resolution amounts to 10 μm and the primary ion current to 1 pA. The structural properties were analyzed with a high resolution x-ray diffractometer (Philips X'Pert MRD) equipped with a 4 × Ge(220) primary monochromator to obtain a highly monochromatic $Cu_{K\alpha}$ beam ($\Delta\lambda/\lambda < 1.5 \cdot 10^{-4}$) and a 3 × Ge(220) analysator with an angular resolution of 11 arc sec in front of a Si-detector. Low-temperature continuous wave (cw) photoluminescence measurements were carried out using a contact gas cryostat and the 244 nm line of a frequency-doubled Ar^+ laser with a power density of 100 mW/cm^2 for excitation. The luminescence signal was recorded using a single channel detector and a spectrometer with 0.1 nm resolution. The Mg content x was determined from the peak energy of the low-temperature $Zn_{1-x}Mg_xO$ PL emission according to the following relation:

$$E_{PL}(4\mathrm{K}) = (3.360 \pm 0.001)\mathrm{eV} + (1.92 \pm 0.04)\mathrm{eV} \cdot x \quad (1)$$

established by averaging over the data given in several publications.[2,28–30] For time resolved PL measurements, a standard streak-camera setup with a 100 fs Ti:sapphire laser as an excitation source was used.[31]

III. EXPERIMENTAL RESULTS

Atomic force microscopy (AFM) reveals smooth surfaces with an RMS roughness between 0.2 nm-0.4 nm and a terrace-like structure with atomic steps with a height of c/2 for both hetero- and homoepitaxial samples (Fig. 1(a)). Figure 1(b) shows the normalized TOF-SIMS Mg profile of simultaneously grown hetero- and homoepitaxial SQW structures. It was found that in heteroepitaxial SQWs, the Mg content of the top $Zn_{1-x}Mg_xO$ barrier only amounts to approximately 65% of the first barrier, whereas for narrow homoepitaxial SQWs, a symmetric barrier structure is obtained. For increasing well width, the Mg content of the top barrier decreases also for homoepitaxial samples but to a significantly smaller extent than for heteroepitaxial samples. The lateral averaging of the primary ion beam with a diameter of 10 μm in combination with the terrace-like surface morphology with peak-to-valley z-values of typically 5 nm for 5 μm × 5 μm images (c.f. Fig. 1(a)) smears out the TOF-SIMS Mg profile. However, the slope of the TOF-SIMS profile at the heterointerfaces is smaller for heteroepitaxial samples, although an AFM analysis yields a similar roughness for both types of samples. Additionally, TOF-SIMS reveals a systematically larger barrier width of the top $Zn_{1-x}Mg_xO$ barrier of about 5 nm compared to the first barrier for heteroepitaxial samples.

To obtain a better understanding of these observations, the structural properties of the investigated samples were studied by high resolution x-ray diffraction (HRXRD). In Figs. 2(a) and 2(b), the ω-rocking-curves of homo- and heteroepitaxial samples are compared. For the symmetric 002 reflex, small full widths at half maximum (FWHMs) close to the resolution of the experimental setup are observed, i.e., 12–22 arc sec for heteroepitaxial and 15–30 arc sec for homoepitaxial samples. The FWHMs of the heteroepitaxial samples are even lower than for homoepitaxial samples which shows that the applied MgO/ZnO double buffer leads to an excellent alignment of the lattice planes perpendicular to the c-axis implying a low density of pure screw-type and mixed dislocations $\leq 2 \cdot 10^6$ cm^{-2}.[2,32] In contrast, the asymmetric 101 ω-rocking-curves of heteroepitaxial samples exhibit large FWHMs of 1400–1700 arc sec, which according to the relations given by Dunn and Kogh,[32] corresponds to an edge-type dislocation density on the order of $\sim 10^{10}$ cm^{-2}. A similar defect structure is also known from the heteroepitaxial growth of GaN on sapphire substrates.[33] The 101 FWHMs of homoepitaxial samples of ~50 arc sec are significantly smaller, and hence, the edge-type dislocation density can be estimated to be $\leq 10^7$ cm^{-2}.

In Fig. 2(c), 002 $2\theta - \omega$-scans of two heteroepitaxial samples of series II are depicted together with best-achieved simulations obtained by using the simulation program GID_sl.[34,35] Pendellösungen are observed for both samples, yet they are more pronounced for the SQW with a well width d_W of 10.4 nm. This points to a higher degree of crystallinity and interface coherence for this sample. The multilayer structure of the samples gives rise to a modulation of the high-frequency oscillations whose oscillation period is mainly

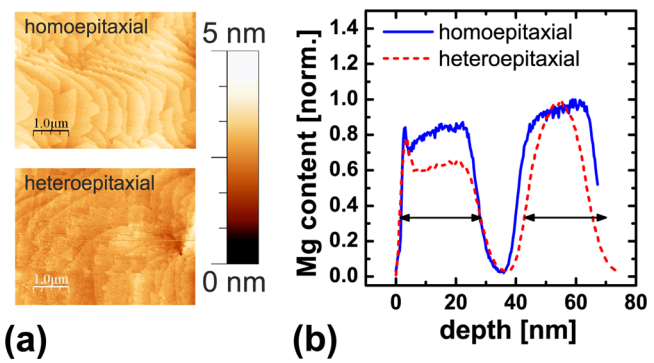

FIG. 1. (Color online) AFM images (a) and TOF-SIMS Mg profiles normalized to 1 (b) of simultaneously grown homo- and heteroepitaxial SQWs. The equally long arrows in (b) illustrate the larger width of the top barrier compared to the first barrier for heteroepitaxial samples.

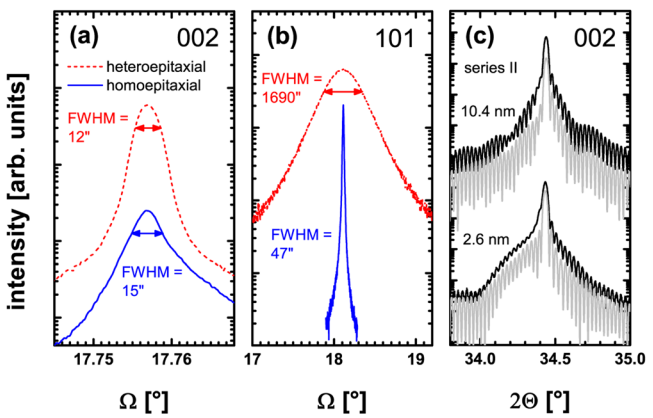

FIG. 2. (Color online) Comparison of (a) symmetric 002 and (b) asymmetric 101 HRXRD ω-rocking-curves of homo- and heteroepitaxial samples, (c) measured (upper curves) and simulated (lower curves) $2\theta - \omega$-scans of two heteroepitaxial SQW structures.

determined by the relatively thick ZnO template layer. A reasonable agreement of experiment and simulation is obtained for the sample with $d_W = 10.4$ nm assuming the following sample structure: ZnO-template ($d = 293$ nm, $c_{ZnO} = 5.2052$ Å) / first ZnMgO barrier ($d = 20$ nm, $c_{ZnMgO} = 5.1997$ Å) / ZnO-well ($d = 10$ nm)/top ZnMgO-barrier ($d = 20$ nm, $c_{ZnMgO} = 5.2025$ Å). Here, the MgO/ZnO double buffer is neglected due to its minor thickness and low crystal quality. The higher value of the *c*-lattice parameter c_{ZnMgO} for the top ZnMgO barrier reflects its lower Mg content. Hence, the HRXRD results confirm the expected layer structure and the TOF-SIMS results. However, the simulation shows deviations from the experimental results particularly on the low-angle side of the 002 diffraction peak. Simulations with an underlying sample structure similar to the one used above completely fail to reproduce the measured diffraction pattern for the sample with a well width d_W of 2.6 nm since this sample exhibits a pronounced shoulder on the low-angle side of the diffraction peak. In order to achieve a good fitting to the measured curve, the top ZnMgO barrier has to be replaced by two layers with the *c* -lattice parameter larger than c_{ZnO}: $c_1 = 5.2245$ Å and $d_1 = 10$ nm/ $c_2 = 5.2199$ Å and $d_2 = 15$ nm. Based on similar observations made for II-VI ZnSe/CdSe quantum wells grown heteroepitaxially on GaAs (Ref. 36), this is interpreted as an indication for a high density of stacking faults created during the growth of the ZnO well or ZnMgO top barrier.

The optical properties of the three sample series are summarized in Fig. 3 comparing the low-temperature PL spectra of all samples under investigation. All samples exhibit sharp bound exciton emission lines that originate from the ZnO template or the bulk ZnO substrate. For heteroepitaxial samples, both the I_6 (3.3608 eV) and the I_9 emission (3.3567 eV) are identified.[37] In contrast, for homoepitaxial samples, the I_9 emission prevails, whose first and second order phonon replicas appear at 3.289 eV and at 3.214 eV, respectively. Additionally, a broad emission from the $Zn_{1-x}Mg_xO$ barrier is observed at higher photon energies (3.45 eV-3.55 eV). The Mg concentration in the lower barrier is determined to $x = 0.085$ ($x = 0.07$) for the heteroepitaxial samples grown at 460 °C (540 °C) and to $x = 0.06$ for the homoepitaxial samples, according to Eq. (1). The emission lines marked by the arrows are attributed to excitonic recombination in the SQW. For wide wells, the SQW emission coincides with the ZnO emission of the template or bulk ZnO substrate. Power-dependent measurements do not reveal any blueshift of the emission energy, and even for large well widths of 9.2 and 10.4 nm, the SQW emission does not drop below the ZnO emission energy, i.e., no indication for the quantum-confined Stark effect (QCSE) was found. For decreasing well width, the SQW emission shifts to higher energies due to quantum confinement. In contrast to homoepitaxial samples, emission lines related to structural defects are observed in the PL spectra of heteroepitaxial samples; the emission line at 3.333 eV found for SQW structures grown at 460 °C (labeled with DBX) is attributed to the recombination of exciton complexes localized at extended defects such as dislocations, dislocation loops, twins, or stacking faults.[37–39] Heteroepitaxial samples grown at 540 °C show a strongly phonon-replicated emission band in the range from 3.31 eV to 3.33 eV. A similar band was observed by Makino *et al.*[17] in single heterostructures and was labeled D-band. We have observed a blueshift of the D-band emission with increasing excitation power, characteristic for a donor-acceptor-pair (DAP) recombination. Temperature-dependent PL measurements reveal pronounced thermal quenching of this emission with an activation energy of 20 meV (Fig. 5(a)), which is explained by the thermal ionization of shallow donors. Due to these properties and the HRXRD results presented above, we assign the D-band to a DAP recombination involving acceptor-like defects confined to basal plane stacking faults, according to Ref. 40. It should be noted that the sample of series II with $d_W = 2.6$ nm, for which the HRXRD $2\theta - \omega$-scan indicates a high density of stacking faults, features a prominent defect-related D-band emission, while the D-band emission of the sample with $d_W = 10.4$ nm is much less pronounced. Furthermore, the sample with $d_W = 2.6$ nm exhibits a more pronounced blueshift and a larger FWHM of the SQW emission than the sample with $d_W = 2.0$ nm, which also features a relatively weak D-band emission. This points to an enhanced Mg diffusion into the quantum well due to the higher density of stacking faults for the sample with $d_W = 2.6$ nm and agrees with the recently reported result that stacking faults act as efficient diffusion

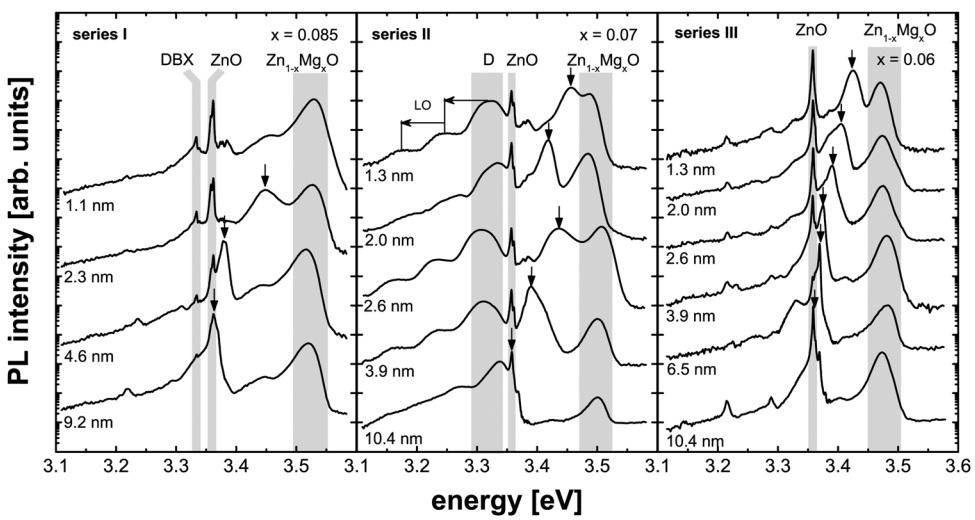

FIG. 3. PL spectra measured at $T = 4.2$ K for SQWs of various well widths heteroepitaxially grown at $T_{Subst} = 460$ °C (series I) and at $T_{Subst} = 540$ °C (series II), as well as homoepitaxially grown at $T_{Subst} = 540$ °C (series III). The SQW emission is marked by arrows. The maximum of the $Zn_{1-x}Mg_xO$ emission was used to determine the Mg concentration x according to Eq. (1). In contrast to homoepitaxial SQWs, emission lines related to extended defects (DBX, D) are observed for heteroepitaxial samples.

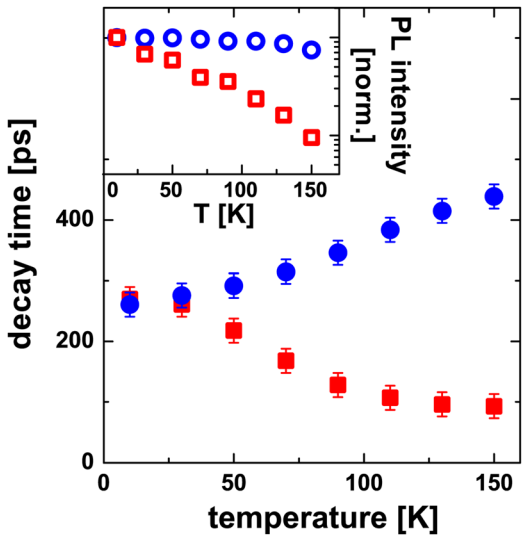

FIG. 4. (Color online) Temperature-dependent PL decay times for the homo- (full circles) and heteroepitaxial SQW (full squares) with a well width of 2.0 nm. The corresponding normalized PL intensities are shown in the inset by the open symbols.

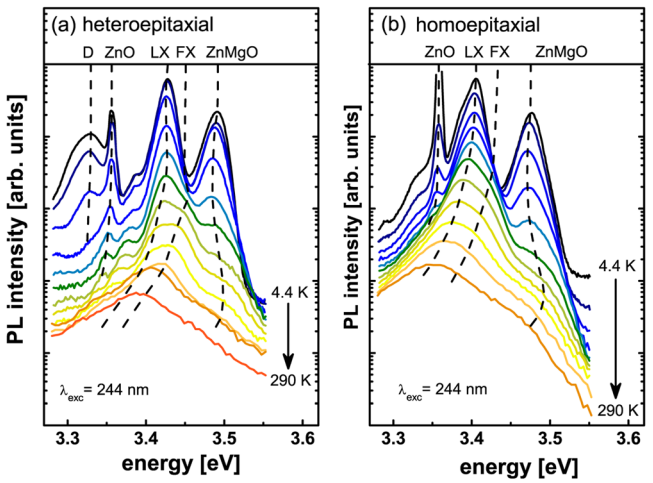

FIG. 5. (Color online) Temperature-dependent PL spectra of a heteroepitaxial (a) and a homoepitaxial SQW (b) with well width $d_W = 2.0$ nm. The SQW emission consists of a contribution from the recombination of LX and from FX, whose peak variation for increasing temperature is represented by the dashed lines (guide for the eye). In the homoepitaxial case, the LX peak prevails up to room temperature. For the heteroepitaxial sample, the D-band disappears for $T > 60$ K.

paths for impurities in ZnMgO.[41] Accordingly, Mg diffusion most probably inhibits the formation of a bound state for the sample with the smallest nominal well width within series I.

In the following, hetero- and homoepitaxial SQW structures grown at 540 °C are compared. The results of time-resolved PL experiments for SQWs of both types with a well width of 2.0 nm are shown in Fig. 4. Here, the 1/e decay time is shown as a function of temperature, and the corresponding integrated PL intensities are plotted in the inset. The decay times for the homo- and heteroepitaxial sample at 4.2 K are similar to literature values of SQWs with comparable well width.[10,42] The simultaneous decrease of the carrier lifetime and PL intensity with increasing temperature in the heteroepitaxial SQW indicates a strong contribution of thermally activated non-radiative recombination channels. In contrast, the homoepitaxial SQW exhibits an almost linearly increasing decay time and constant PL intensity when the lattice temperature is increased. The PL dynamics in the temperature regime below 170 K are, therefore, mainly governed by radiative recombination and carrier cooling processes.[43]

Temperature-dependent cw-PL spectra for the homo- and heteroepitaxial SQW with a d_W of 2.0 nm are shown in Fig. 5. The $Zn_{1-x}Mg_xO$ barrier emission shows a S-shape with temperature typically assigned to alloy disorder.[2,7,31,44] The SQW emission consists of two different peaks, labeled localized excitons (LX) and free excitons (FX). We attribute the FX peak to the recombination of free excitons and the LX peak to the recombination of excitons localized to well width and barrier height fluctuations or extrinsic impurities. While for the heteroepitaxial SQW the FX peak becomes dominant for temperatures above 160 K, for the homoepitaxial sample, the LX peak prevails up to room temperature and the FX peak appears only as a shoulder on its high-energy side. This observation applies also to the homoepitaxial SQWs with a well width of 2.6 nm and 3.9 nm. The temperature dependence of the integrated SQW emission intensity in Fig. 5 is fitted using a two-step dissociation model[45]

$$I(T) = I_0 \cdot \left(1 + C_1 \exp\left(\frac{-E_1}{kT}\right) + C_2 \exp\left(\frac{-E_2}{kT}\right)\right)^{-1}, \quad (2)$$

with the fitting coefficients I_0, C_1, and C_2 and the activation energies E_1 and E_2. This is exemplarily shown for two SQWs samples in Fig. 6(b). The fitting results for all samples are summarized in Table I. E_1 represents the dominant non-radiative process for the low-temperature regime and ranges between 5 meV and 16 meV except for the thinnest homoepitaxial SQW, for which an activation energy of 35 meV is derived. In that case, no value for E_2 can be determined as the corresponding non-radiative process prevails up to room temperature. The activation energy E_2 is associated with the dominant non-radiative recombination process above 160 K. For heteroepitaxial samples, the values obtained are close to the exciton binding energy in bulk ZnO, for which a value of 59 meV has been reported.[46] Significantly higher values of E_2 are obtained for homoepitaxial samples with 2 nm $\leq d_W \leq 4$ nm, which is approximately twice the exciton Bohr radius of 1.8 nm.[17] The enhanced thermal stability of excitons in homo- compared to heteroepitaxial SQWs is also reflected by an almost five times higher room temperature luminescence intensity of the former.

IV. DISCUSSION

The HRXRD and PL results demonstrate the improved structural quality of homo- compared to heteroepitaxial SQW structures. Especially, a suppression of non-radiative processes below 170 K is observed in the time-resolved PL measurements. Additionally, for homoepitaxial samples, both the symmetric 002 and the asymmetric 101 ω-rocking-curves exhibit narrow FWHMs. In contrast, defect-related PL emission lines like the DBX-line and the D-band are observed in low-temperature PL spectra of heteroepitaxial samples. Since the intensity of the D-band is commonly significantly lower in

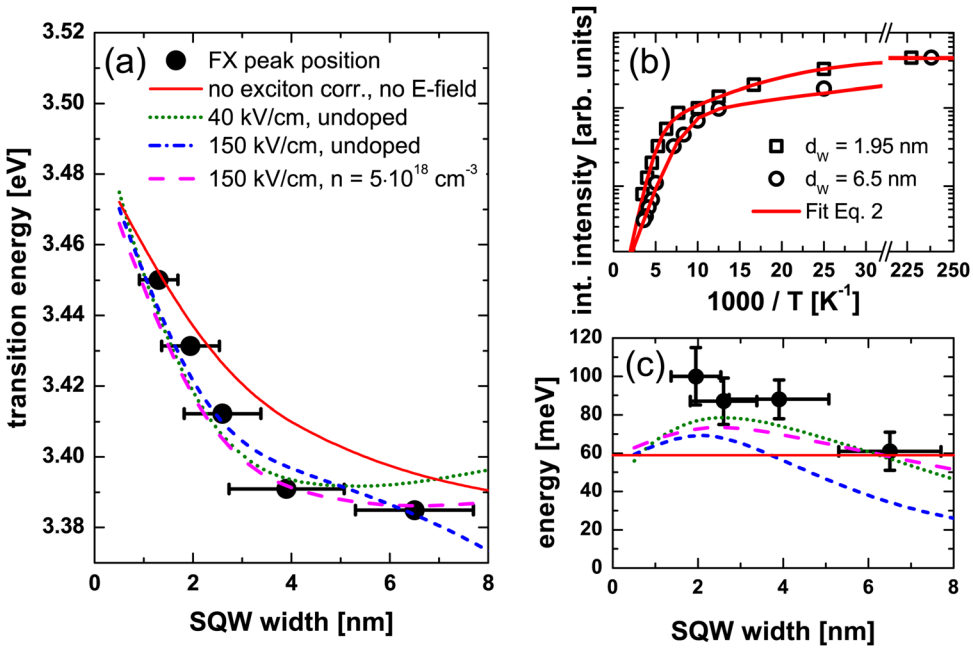

FIG. 6. (Color online) (a) FX transition energy of homoepitaxial SQWs at 4.2 K (full circles). The experimental values are compared to simulations performed using nextnano[3] without internal electric field and with a constant exciton binding energy (continuous line), for an internal field of 40 kV/cm (dotted line) and 150 kV/cm (short-dashed line) including a well width dependent correction of the exciton binding energy as well as for a field of 150 kV/cm with a residual charge carrier concentration of $n = 5 \cdot 10^{18}\,\mathrm{cm}^{-3}$ (long-dashed line). (b) Determination of the activation energies E_1 and E_2 for two homoepitaxial SQWs with well widths d_W of 2.0 nm and 6.5 nm by fitting the integrated PL intensity with Eq. (2). (c) Exciton binding energy calculated according to Ref. 52 (line style as in (a)) and plotted alongside the activation energies E_2. The continuous line marks the exciton binding energy in bulk ZnO.

single heterostructures than in SQWs and based on the analysis of the $2\theta - \omega$-scans presented above, it can be concluded that stacking faults are predominantly generated during the growth of the ZnO quantum well and the top ZnMgO barrier. Due to their low formation energy, stacking faults are common defects in ZnO,[47] often induced by biaxial strain[41] or generated by the precipitation of interstitial atoms under non-stoichiometric growth conditions[48,49] or during incorporation of dopants.[50] When growing ZnMgO on ZnO, a phase transition from wurtzite to rock-salt occurs when increasing the Mg content above a critical value, that depends on the actual growth conditions and the employed substrate. As the Mg content of the samples investigated here are close to this critical value, we surmise that the generation of stacking faults can be regarded as a first indication for the onset of the wurtzite-to-cubic phase-transition and that the stacking fault density critically depends on the exact Mg content. Furthermore, we suspect that the higher density of edge-type dislocations as well as other extended defects (DBX-line) in heteroepitaxial samples facilitates the formation of stacking faults since grain boundaries between neighboring columnar grains are known to be one origin for the formation of stacking faults[51] and since the formation energy of accompanying partial dislocations is lowered.[50,51] A TOF-SIMS analysis suggests that the formation of stacking faults leads to a lower Mg content and a larger width of the top $Zn_{1-x}Mg_xO$ barrier. This is explained by defect-enhanced interdiffusion of quantum well and top barrier and by a higher growth rate due to an improved Zn incorporation. The latter effect can be attributed to the precipitation of interstitial Zn atoms often reported to be a plausible mechanism for the generation of stacking faults.[49–51] The resulting reduction of the top barrier height weakens the quantum confinement in heteroepitaxial SQWs, and consequently, no enhancement of the exciton binding energy is observed. Mg diffusion from the barriers into the well facilitated by structural defects is assumed to inhibit the formation of a bound state in narrow SQWs (series I) or to cause a significant blueshift ($d_W = 2.6$ nm, series II).

TABLE I. Activation energies E_1 and E_2 obtained by fitting the temperature dependence of the integrated PL intensity of simultaneously grown homo- and heteroepitaxial SQWs with Eq. (2).

Well width	Heteroepitaxial		Homoepitaxial	
(nm)	E_1(meV)	E_2(meV)	E_1(meV)	E_2(meV)
1.3	8.0 ± 2.0	60 ± 7	35 ± 1.0	–
2.0	16.0 ± 0.4	58 ± 8	11.7 ± 0.4	100 ± 12
2.6	–	–	8.0 ± 1.0	87 ± 12
3.9	10.4 ± 0.9	63 ± 7	10.0 ± 1.4	88 ± 10
6.5	–	–	4.0 ± 0.8	61 ± 10

In Fig. 6(a), the SQW FX emission energies of homoepitaxial SQWs as a function of the well width are compared to the results of numerical simulations performed using nextnano[3] with the material parameters given in Refs. 53, 62, and 63. Simulations were performed for the absence of an internal electric field and assuming a constant exciton binding energy of 59 meV (red continuous line). The role of internal electric fields for SQWs with a low Mg concentration $x \leq 0.1$ is still under debate: Park and Ahn[54] and Tsukazaki *et al.*[55] argue that spontaneous and piezoelectric polarization almost compensate for low Mg concentrations and that due to bowing of the *a*-lattice parameter polarization-induced electric fields only become relevant for Mg concentrations

$x > 0.1$. According to these authors, the internal field for an Mg concentration $x = 0.06$ is estimated to ≤ 40 kV/cm. In contrast, in Refs. 12 and 18, a linear increase of the overall polarization with Mg content is suggested, giving rise to considerably larger built-in electric fields for $x = 0.06$. Therefore, simulations for various internal electric fields E_{int} were performed to explain our experimental data. Figure 6 displays the results for $E_{int} = 40$ kV/cm (green dotted line) and for $E_{int} = 150$ kV/cm (blue short-dashed line). In the calculation of the transition energies, the variation of the exciton binding energy for different well widths according to the method proposed in Ref. 52 (c.f. Fig. 6(c)) was included. This leads to a significantly better agreement with the experimental data for well widths $2\,\text{nm} \leq d_W \leq 6\,\text{nm}$, as otherwise, the simulation systematically overestimates the experimental transition energies.[17,56] Moreover, Fig. 6(a) reveals that built-in fields up to 150 kV/cm have only little impact on the transition energies for well widths $d_W \leq 5$ nm. In the case of a small internal electric field of 40 kV/cm, the apparent decrease of the exciton binding energy due to the charge separation prevails over the field-induced redshift. Therefore, the transition energy slightly increases for larger well widths. This does not apply for fields >150 kV/cm, and thus, a decrease of the transition energy for wider wells is obtained. A distinct effect of internal electric fields on the optical transition energies of the samples under investigation here is only expected for well widths $d_W \geq 5$ nm. Therefore, in Fig. 6(c), their influence on the exciton binding energy is shown and compared to the activation energies E_2 obtained by fitting the integrated PL intensity according to Eq. (2) (Fig. 6(b)). For small internal electric fields, the increase of E_2 with well width $2\,\text{nm} \leq d_W \leq 4\,\text{nm}$ for the homoepitaxial samples is partially explained by quantum confinement. Yet, an increase of the transition energies for larger wells is not observed in the experiments. A good agreement of the experimental and calculated transition energies is obtained for an internal electric field of 150 kV/cm, however, the calculated values for the exciton binding energy are smaller than the activation energies E_2. The best agreement of calculations and experimental data is achieved by including a background charge carrier concentration, which screens internal electric fields. The simulations show that for a built-in field of 150 kV/cm, a residual doping concentration of $n = 5 \cdot 10^{18}\text{cm}^{-3}$ is necessary. In Refs. 57 and 58, it is shown that, due to the segregation of group-III impurities acting as shallow donors in ZnO, charge carriers accumulate near the surface. The observation of the I_6 and I_9 lines associated to Al and In impurities[37] and the small thickness of the $Zn_{1-x}Mg_xO$ top barrier of 20 nm, therefore, suggest that internal electric fields are partially screened by unintentional doping. Based on these results, we conclude that up to now the QCSE in $ZnO/Zn_{1-x}Mg_xO$ SQWs with $x \leq 0.12$ (Refs. 7,10,19,59) could not be observed due to screening by unintentional doping and the reduction of the exciton binding energy by the charge separation in the well. In heteroepitaxial SQWs, the influence of built-in fields is additionally concealed by an asymmetric barrier structure and possible defect-induced Mg indiffusion. The bowing of the *a*-lattice parameter observed by Park and Ahn[54] and Tsukazaki *et al.*[55], and that was proposed to be the reason for spontaneous and piezoelectric polarization to compensate for Mg concentrations $x \leq 0.1$, is most likely an effect of the growth on a-plane sapphire applied in that work. Since the quadruple of the *a*-lattice parameter of ZnO is almost identical to the *c*-lattice parameter of sapphire $c_{sapphire} \approx 4 \cdot a_{ZnO}$,[60] for low Mg concentrations, $Zn_{1-x}Mg_xO$ forms a coincidence lattice with the a-plane sapphire substrate. By increasing the Mg concentration, the *a*-lattice parameter increases, and therefore, a transition from strained to relaxed growth occurs giving rise to the observed bowing.

According to Fig. 6(c), the calculated increase of the exciton binding energy due to an enhanced overlap of electron and hole wave functions cannot fully explain the large values of the activation energies E_2 for well widths $2\,\text{nm} \leq d_W \leq 4\,\text{nm}$. We attribute this to the localization of excitons to potential fluctuations which plays an important role in ZnO due to the small exciton Bohr radius. In SQWs with pronounced confinement, the energetic splitting of the LX and the FX peaks increases and hence gives rise to exciton localization up to room temperature. Therefore, E_2 involves both the exciton binding energy and the localization energy for homoepitaxial samples. The linearly increasing decay time for $T \leq 170$ K points towards exciton localization at well width or barrier height fluctuations, because in that case, wave vector conservation is not completely relaxed. However, localization to extrinsic impurities cannot be ruled out since it is difficult in time-resolved PL experiments to spectrally separate between LX and FX. Also in thermal equilibrium, the FX recombination is a decay channel for chemically bound excitons. Therefore, the increase of the FX radiative life time due to the extension of occupied states in momentum space for higher temperatures entails an increase of the decay time of bound excitons in case the radiative recombination prevails.[61]

V. SUMMARY

A comprehensive comparison of structural and optical properties of hetero- and homoepitaxial $ZnO/Zn_{1-x}Mg_xO$ SQWs demonstrates the benefits of homoepitaxial growth. HRXRD and low-temperature PL measurements indicate a significantly higher density of extended structural defects, especially the generation of stacking faults during the SQW growth in the heteroepitaxial case. In contrast, for homoepitaxial samples, symmetric $Zn_{1-x}Mg_xO$ barriers are obtained, effectively confining excitons in the quantum well. This leads to a suppression of non-radiative recombination below 170 K and to an enhanced temperature stability of the SQW emission for homoepitaxially grown samples due to the enhanced overlap of electron and hole wave functions and due to exciton localization up to room temperature. The influence of polarization-induced electric fields was studied in detail comparing experimental transition and activation energies to simulations. Thereby, several influencing factors were identified which inhibit the observation of the QCSE effect for low Mg concentrations: the decrease of the exciton binding energy counteracting the field-induced redshift, screening by unintentional doping as well as reduced Mg incorporation in the top barrier, and Mg diffusion into heteroepitaxial SQWs.

ACKNOWLEDGMENTS

The authors would like to thank Stefan Birner from the Walter Schottky Institut for his support with the nextnano[3] simulations. Furthermore, financial support by the Deutsche Forschungsgemeinschaft via NAWACS (EI 518/2–1) and by the EU via the FP 7 Integrated Project ORAMA (CP-IP 246334-2) is gratefully acknowledged. B.L. acknowledges financial support from the Universität Bayern e.V.

[1]A. Ohtomo, M. Kawasaki, T. Koida, K. Masubuchi, H. Koinuma, Y. Sakurai, Y. Yoshida, T. Yasuda, and Y. Segawa, Appl. Phys. Lett. **72**, 2466 (1998).
[2]T. A. Wassner, B. Laumer, S. Maier, A. Laufer, B. K. Meyer, M. Stutzmann, and M. Eickhoff, J. Appl. Phys. **105**, 023505 (2009).
[3]H. Matsui, H. Tabata, N. Hasuike, and H. Harima, J. Appl. Phys. **99**, 024902 (2006).
[4]T. Makino, K. Tamura, C. H. Chia, Y. Segawa, M. Kawasaki, A. Ohtomo, and H. Koinuma, Appl. Phys. Lett. **81**, 2172 (2002).
[5]H. Tampo, H. Shibata, K. Matsubara, A. Yamada, P. Fons, S. Niki, M. Yamagata, and H. Kanie, Appl. Phys. Lett. **89**, 132113 (2006).
[6]M. Yano, K. Hashimoto, K. Fujimoto, K. Koike, S. Sasa, M. Inoue, Y. Uetsuji, T. Ohnishi, and K. Inaba, J. Cryst. Growth **301-302**, 353 (2007).
[7]T. Gruber, C. Kirchner, R. Kling, F. Reuss, and A. Waag, Appl. Phys. Lett. **84**, 5359 (2004).
[8]C. Morhain, T. Bretagnon, P. Lefebvre, X. Tang, P. Valvin, T. Guillet, B. Gil, T. Taliercio, M. Teisseire-Doninelli, B. Vinter, and C. Deparis, Phys. Rev. B **72**, 241305 (2005).
[9]S. Sadofev, S. Blumstengel, J. Cui, J. Puls, S. Rogaschewski, P. Schäfer, Y. G. Sadofyev, and F. Henneberger, Appl. Phys. Lett. **87**, 091903 (2005).
[10]B. P. Zhang, N. T. Binh, K. Wakatsuki, C. Y. Liu, Y. Segawa, and N. Usami, Appl. Phys. Lett. **86**, 032105 (2005).
[11]M. Al-Suleiman, A. El-Shaer, A. Bakin, H.-H. Wehmann, and A. Waag, Appl. Phys. Lett. **91**, 081911 (2007).
[12]T. Bretagnon, P. Lefebvre, T. Guillet, T. Taliercio, B. Gil, and C. Morhain, Appl. Phys. Lett. **90**, 201912 (2007).
[13]J.-M. Chauveau, M. Laügt, P. Venneguès, M. Teisseire, B. Lo, C. Deparis, C. Morhain, and B. Vinter, Semicond. Sci. Technol. **23**, 035005 (2008).
[14]T. Makino, Y. Segawa, A. Tsukazaki, A. Ohtomo, and M. Kawasaki, Appl. Phys. Lett. **93**, 121907 (2008).
[15]M. Brandt, M. Lange, M. Stölzel, A. Müller, G. Benndorf, J. Zippel, J. Lenzner, M. Lorenz, and M. Grundmann, Appl. Phys. Lett. **97**, 052101 (2010).
[16]J. Zippel, J. Lenzner, G. Benndorf, M. Lange, H. Hochmuth, M. Lorenz, and M. Grundmann, J. Vac. Sci. Technol. B **27**, 1735 (2009).
[17]T. Makino, C. H. Chia, N. T. Tuan, H. D. Sun, Y. Segawa, M. Kawasaki, A. Ohtomo, K. Tamura, and H. Koinuma, Appl. Phys. Lett. **77**, 975 (2000).
[18]K. Koike, G.-Y. Takada, K. Fujimoto, S. Sasa, M. Inoue, and M. Yano, in *Proceedings of the 12th International Conference on Modulated Semiconductor Structures* [Physica E (Amsterdam) **32**, 191 (2006)].
[19]X. Q. Gu, L. P. Zhu, Z. Z. Ye, H. P. He, Y. Z. Zhang, F. Huang, M. X. Qiu, Y. J. Zeng, F. Liu, and W. Jaeger, Appl. Phys. Lett. **91**, 022103 (2007).
[20]J. Zhu, A. Y. Kuznetsov, M.-S. Han, Y.-S. Park, H.-K. Ahn, J.-W. Ju, and I.-H. Lee, Appl. Phys. Lett. **90**, 211909 (2007).
[21]H. Matsui, H. Saeki, T. Kawai, A. Sasaki, M. Yoshimoto, M. Tsubaki, and H. Tabata, J. Vac. Sci. Technol. B **22**, 2454 (2004).
[22]C. Neumann, S. Lautenschläger, S. Graubner, J. Sann, N. Volbers, B. K. Meyer, J. Blsing, A. Krost, F. Bertram, and J. Christen, Phys. Status Solidi B **244**, 1451 (2007).
[23]H. von Wenckstern, H. Schmidt, C. Hanisch, M. Brandt, C. Czekalla, G. Benndorf, G. Biehne, A. Rahm, H. Hochmuth, M. Lorenz, and M. Grundmann, Physica Status Solidi (RRL) **1**, 129 (2007).
[24]Y. Chen, H.-J. Ko, S.-K. Hong, and T. Yao, Appl. Phys. Lett. **76**, 559 (2000).
[25]A. Bakin, A. El-Shaer, A. C. Mofor, M. Kreye, A. Waag, F. Bertram, J. Christen, M. Heuken, and J. Stoimenos, in *Proceedings of the International Conference on Materials for Advanced Technologies* (ICMAT 2005) Symposium N - ZnO and Related Materials [J. Cryst. Growth **287**, 7 (2006)].
[26]The used bulk ZnO substrates were purchased by CrysTec GmbH, see http://www.crystec.de.
[27]S. Graubner, C. Neumann, N. Volbers, B. K. Meyer, J. Bläsing, and A. Krost, Appl. Phys. Lett. **90**, 042103 (2007).
[28]M. Lorenz, M. Brandt, M. Lange, G. Benndorf, H. von Wenckstern, D. Klimm, and M. Grundmann, in *Proceedings of the EMRS 2009 Spring Meeting Symposium H: Synthesis, Processing and Characterization of Nanoscale Multi Functional Oxide Films II* [Thin Solid Films **518**, 4623 (2010)].
[29]H. Shibata, H. Tampo, K. Matsubara, A. Yamada, K. Sakurai, S. Ishizuka, S. Niki, and M. Sakai, Appl. Phys. Lett. **90**, 124104 (2007).
[30]S. Heitsch, G. Zimmermann, D. Fritsch, C. Sturm, R. Schmidt-Grund, C. Schulz, H. Hochmuth, D. Spemann, G. Benndorf, B. Rheinländer, T. Nobis, M. Lorenz, and M. Grundmann, J. Appl. Phys. **101**, 083521 (2007).
[31]A. Chernikov, S. Horst, M. Koch, K. Volz, S. Chatterjee, S. Koch, T. Wassner, B. Laumer, and M. Eickhoff, J. Lumin. **130**, 2256 (2010).
[32]C. Dunn and E. Kogh, Acta Metall. **5**, 548 (1957).
[33]B. Heying, X. H. Wu, S. Keller, Y. Li, D. Kapolnek, B. P. Keller, S. P. DenBaars, and J. S. Speck, Appl. Phys. Lett. **68**, 643 (1996).
[34]See http://sergey.gmca.aps.anl.gov/gidsl.html. for information about the simulation program GID_sl.
[35]S. Stepanov and R. Kohler, J. Phys. D: Appl. Phys. **27**, 1922 (1994).
[36]T. Passow, K. Leonardi, A. Stockmann, H. Selke, H. Heinke, and D. Hommel, J. Phys. D: Appl. Phys. **32**, A42 (1999).
[37]B. K. Meyer, H. Alves, D. M. Hofmann, W. Kriegseis, D. Forster, F. Bertram, J. Christen, A. Hoffmann, M. Straburg, M. Dworzak, U. Haboeck, and A. V. Rodina, Phys. Status Solidi B **241**, 231 (2004).
[38]M. R. Wagner, G. Callsen, J. S. Reparaz, J.-H. Schulze, R. Kirste, M. Cobet, I. A. Ostapenko, S. Rodt, C. Nenstiel, M. Kaiser, A. Hoffmann, A. V. Rodina, M. R. Phillips, S. Lautenschläger, S. Eisermann, and B. K. Meyer, Phys. Rev. B **84**, 035313 (2011).
[39]P. J. Dean, Phys. Status Solidi A **81**, 625 (1984).
[40]M. Schirra, R. Schneider, A. Reiser, G. M. Prinz, M. Feneberg, J. Biskupek, U. Kaiser, C. E. Krill, K. Thonke, and R. Sauer, Phys. Rev. B **77**, 125215 (2008).
[41]J. Pierce, H. Wen, K. Liu, M. Kumrr, J. Tresback, Y. Ali, A. Krahnert, and B. Adekore, J. Cryst. Growth **325**, 20 (2011).
[42]T. V. Shubina, A. A. Toropov, O. G. Lublinskaya, P. S. Kop'ev, S. V. Ivanov, A. El-Shaer, M. Al-Suleiman, A. Bakin, A. Waag, A. Voinilovich, E. V. Lutsenko, G. P. Yablonskii, J. P. Bergman, G. Pozina, and B. Monemar, Appl. Phys. Lett. **91**, 201104 (2007).
[43]C. F. Klingshirn, *Semiconductor Optics* (Springer, Berlin, Heidelberg, New York, 2007).
[44]A. Bell, S. Srinivasan, C. Plumlee, H. Omiya, F. A. Ponce, J. Christen, S. Tanaka, A. Fujioka, and Y. Nakagawa, J. Appl. Phys. **95**, 4670 (2004).
[45]D. Bimberg, M. Sondergeld, and E. Grobe, Phys. Rev. B **4**, 3451 (1971).
[46]D. G. Thomas, J. Phys. Chem. Solids **15**, 86 (1960).
[47]Y. Yan, G. M. Dalpian, M. M. Al-Jassim, and S.-H. Wei, Phys. Rev. B **70**, 193206 (2004).
[48]J. Narayan, K. Dovidenko, A. K. Sharma, and S. Oktyabrsky, J. Appl. Phys. **84**, 2597 (1998).
[49]D. Gerthsen, D. Litvinov, T. Gruber, C. Kirchner, and A. Waag, Appl. Phys. Lett. **81**, 3972 (2002).
[50]A. Allenic, W. Guo, Y. B. Chen, Y. Che, Z. D. Hu, B. Liu, and X. Q. Pan, J. Phys. D: Appl. Phys. **41**, 025103 (2008).
[51]Z. Zhang, C. Bao, S. Ma, and S. Hou, Appl. Surf. Sci. **257**, 7893 (2011).
[52]R. P. Leavitt and J. W. Little, Phys. Rev. B **42**, 11774 (1990).
[53]The parameters used in the simulation are $m_{e\perp} = 0.24\ m_0$, $m_{e\parallel} = 0.28\ m_0$, $m_{h\perp} = 0.54\ m_0$, and $m_{h\parallel} = 2.74\ m_0$ for the mass of the conduction (valence) band electrons (holes) perpendicular and parallel to the c-direction (See also Ref. 62). For the static dielectric constant, $\varepsilon_\perp = 7.77$ and $\varepsilon_\parallel = 8.91$ were used (See also Ref. 63). These parameters were also employed for $Zn_{1-x}Mg_xO$ which is a reasonable approximation due to the low Mg content of the SQW barriers. According to Ref. 56, the conduction to valence band offset ratio of ZnO and $Zn_{1-x}Mg_xO$ was chosen to be 65/35. For the calculation of the exciton binding energy, an exciton Bohr radius aB of 1.8 nm was used.[17]
[54]S.-H. Park and D. Ahn, Appl. Phys. Lett. **87**, 253509 (2005).
[55]A. Tsukazaki, A. Ohtomo, T. Kita, Y. Ohno, H. Ohno, and M. Kawasaki, Science **315**, 1388 (2007).
[56]G. Coli and K. K. Bajaj, Appl. Phys. Lett. **78**, 2861 (2001).
[57]D. Taïnoff, M. Al-Khalfioui, C. Deparis, B. Vinter, M. Teisseire, C. Morhain, and J.-M. Chauveau, Appl. Phys. Lett. **98**, 131915 (2011).
[58]D. C. Look, B. Claflin, and H. E. Smith, Appl. Phys. Lett. **92**, 122108 (2008).

[59]T. Makino, K. Tamura, C. H. Chia, Y. Segawa, M. Kawasaki, A. Ohtomo, and H. Koinuma, Appl. Phys. Lett. **81**, 2355 (2002).
[60]P. Fons, K. Iwata, A. Yamada, K. Matsubara, S. Niki, K. Nakahara, T. Tanabe, and H. Takasu, Appl. Phys. Lett. **77**, 1801 (2000).
[61]F.-Y. Jen, Y.-C. Lu, C.-Y. Chen, H.-C. Wang, C. C. Yang, B.-P. Zhang, and Y. Segawa, Appl. Phys. Lett. **87**, 252117 (2005).
[62]W. R. L. Lambrecht, A. V. Rodina, S. Limpijumnong, B. Segall, and B. K. Meyer, Phys. Rev. B **65**, 075207 (2002).
[63]N. Ashkenov, B. N. Mbenkum, C. Bundesmann, V. Riede, M. Lorenz, D. Spemann, E. M. Kaidashev, A. Kasic, M. Schubert, M. Grundmann, G. Wagner, H. Neumann, V. Darakchieva, H. Arwin, and B. Monemar, J. Appl. Phys. **93**, 126 (2003).